American Mineralogist, Volume 87, pages 1096–1103, 2002

Protoanthophyllite from three metamorphosed serpentinites

HIROMI KONISHI,[1,*] ISTVÁN DÓDONY,[1,†] AND PETER R. BUSECK[1,2]

[1]Department of Geological Sciences, Arizona State University, Tempe, Arizona 85287-1404, U.S.A.
[2]Department of Chemistry/Biochemistry, Arizona State University, Tempe, Arizona 85287-1604, U.S.A.

ABSTRACT

This is the first report of a natural Mg-rich protoanthophyllite. It is common in metamorphosed serpentinites from three Japanese ultramafic complexes, and some crystals contain anthophyllite (*Pnma*) lamellae. The Mg/(Mg + Fe) ratios of the Hayachine, Tari-Misaka, and Takase protoanthophyllites are 0.90, 0.92, and 0.91, respectively. The samples have identical optical properties: $X = \mathbf{a}$, $Y = \mathbf{b}$, $Z = \mathbf{c}$, and $2V_x = 64 \pm 5°$. Their space group is *Pnmn* (or *Pn*2*n*), as revealed by systematic extinctions in selected-area electron-diffraction patterns. The protoanthophyllite and anthophyllite have similar compositions and orthorhombic symmetry. They are difficult to distinguish using optical, microanalytical, and powder X-ray diffraction measurements. This problem raises the possibility that some of the published data on geological and synthetic anthophyllite samples may be of misidentified materials, potentially leading to errors in the published stability relations of anthophyllite. We provide a method to identify protoanthophyllite and differentiate it from its polymorphs using selected-area electron diffraction and high-resolution transmission electron microscopy methods.

INTRODUCTION

Members of the anthophyllite–gedrite amphibole series are significant minerals for petrological studies of metamorphic rocks. They occur in metamorphosed ultramafic rocks, in reaction zones between ultramafic and country rocks, in low-Ca amphibolites, and in iron formations (Robinson et al. 1982; Deer et al. 1997). When ultramafic rocks are incorporated into orogenic belts by obduction or subduction, they commonly are hydrated to serpentinite and then recrystallized under various metamorphic conditions (Spear 1993). Anthophyllite occurs in Alpine-type peridotites (e.g., Evans and Trommsdorff 1970; Trommsdorff and Evans 1972), and anthophyllite and gedrite are essential components in cordierite-anthophyllite rocks, which contain assemblages that are characteristic of specific *P-T* conditions (Spear 1993). The association of kyanite or sillimanite with Al-bearing anthophyllite or gedrite represents moderately high-pressure metamorphic conditions (>~5 kbar) (Spear 1993), and Liu and Liou (1995) reported a high-pressure kyanite and Al-bearing anthophyllite schist that is associated with the Dabie Mountains ultrahigh-pressure metamorphic rocks in China.

Metamorphic reactions of serpentinites have been studied extensively. With increasing temperature, there are associations of serpentine–brucite ± diopside, serpentine–olivine ± diopside, serpentine–olivine ± tremolite, olivine–talc ± tremolite, olivine–anthophyllite ± tremolite, olivine–enstatite ± tremolite, and olivine–enstatite ± diopside (Evans and Trommsdorff 1970; Tracy and Frost 1991; Spear 1993). As shown by Evans and Trommsdorff (1970), anthophyllite can be produced by the reaction:

$$4 \text{ olivine} + 9 \text{ talc} = 5 \text{ anthophyllite} + 4\, H_2O \qquad (1)$$

The reaction:

$$\text{anthophyllite} + \text{olivine} = 9 \text{ enstatite} + H_2O \qquad (2)$$

marks the upper thermal stability of anthophyllite. Both reactions have steep slopes in the *P-T* diagram, making them good indicators of temperature (~600–700 °C) (Evans and Trommsdorff 1970; Tracy and Frost 1991).

The structure of anthophyllite [$(Mg,Fe)_7Si_8O_{22}(OH)_2$], like that of other amphiboles, can be viewed as consisting of bands of SiO_4 tetrahedra and (Mg, Fe)-centered octahedra parallel to **c**. These bands can be understood in terms of the I-beam model of Papike and Ross (1970) and Thompson (1970). Two tetrahedral and one octahedral band comprise an I-beam. The arrangement of I-beams forms alternating layers of tetrahedra and octahedra parallel to (100). The octahedral layers can have either of two orientations, with one related to the other by a half-rotation around the **c** axis. Different octahedral orientations between adjacent tetrahedral layers cause different stacking sequences. The stacking vector between neighboring tetrahedral layers is +**c**/3 or –**c**/3 or, more simply, + or – (Hawthorne 1981). In anthophyllite, like in other *Pnma* amphiboles, the stacking vector in alternate paired tetrahedral layers reverses (…++– –…).

The various combinations of stacking vectors along the **a** axis results in different amphibole polymorphs (Fig. 1, left column). The same orientation (...++++… or … – – – – …) of tetrahedral layers produces the clinoamphibole structure with

---

* E-mail: hkonishi85282@hotmail.com

† Permanent address: Department of Mineralogy, Eötvös L. University, Pázmány Péter sétány 1/C, Budapest, H-1117, Hungary.

0003-004X/02/0809–1096$05.00

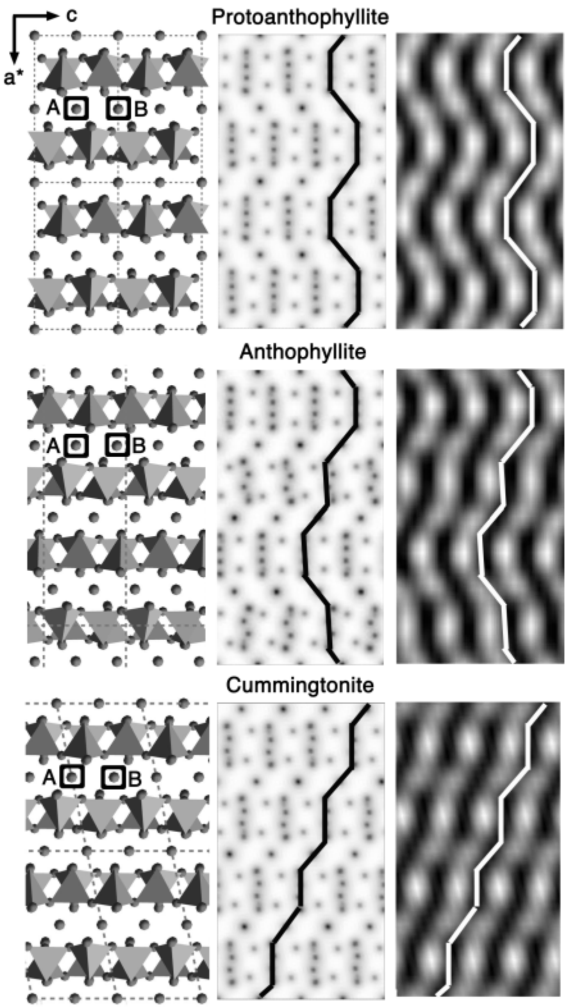

FIGURE 1. Crystal structures (left) of Mg-Fe amphibole polymorphs, the corresponding projected-potential images (middle) for thicknesses of 1**b**, and simulated HRTEM images (right) for thicknesses of ~11 nm and a defocus value of –40.5 nm. The Si and superimposed O positions of SiO_4 tetrahedra and M octahedral sites are linked by dark or white line in the projected-potential images and simulated HRTEM images. M1 and M2 sites superimpose M4 and M3 sites, respectively, and the M2/M3 and M1/M4 positions are labeled A and B, respectively. The ratio of occupied sites in the M2/M3 column to those in the M1/M4 column is 3/4, resulting in the slightly lower intensities at M2/M3 positions in the simulated HRTEM images. The dashed lines in the left column mark unit cells.

symmetry $C2/m$ or $P2_1/m$, e.g., cummingtonite [$(Mg,Fe)_7Si_8O_{22}(OH)_2$]. Reversal of stacking vectors in alternate tetrahedral layers (…+–+–…) produces *Pnmn* amphiboles. In this paper we shall, consistent with general usage, call the *Pnmn* polymorph protoamphibole. We will also use the mineral names protoanthophyllite, anthophyllite, cummingtonite, and gedrite, following the amphibole nomenclature (Leake et al. 1997).

Protoamphibole (stacking sequence …+–+–…) was first described as a synthetic F- and Li-bearing species [$Na_{0.03}Li_{1.40}Mg_{6.44}Si_{7.84}Al_{0.04}O_{21.71}F_{2.14}(OH)_{0.15}$] (Gibbs et al. 1960; Gibbs 1969). Recently, natural protoamphiboles (Fe- and Mn-, Fe-bearing species protoferro-anthophyllite and protomangano-ferro-anthophyllite) were discovered in three pegmatites and one manganese deposit (Sueno et al. 1998). We have observed high-resolution transmission electron microscopy (HRTEM) images and selected-area electron-diffraction (SAED) patterns of Mg-Fe amphiboles from three serpentinites in Japan that are inconsistent with anthophyllite, and evidence suggests that they are protoanthophyllite.

Our goals are to describe these first occurrences of protoanthophyllite and to provide reliable SAED and HRTEM criteria to distinguish among the various polymorphs. We speculate that protoanthophyllite might be misidentified as anthophyllite in some publications on natural and synthetic amphiboles because of their similar compositions, optical properties, and powder X-ray diffraction (XRD) patterns. Therefore, it might be appropriate to reexamine both the stability relations of anthophyllite and the estimated *P-T* conditions of metamorphic rocks containing anthophyllite.

GEOLOGICAL SETTING AND SAMPLES

Serpentinites ranging from one to several kilometers wide are common in the Japanese islands, and most have experienced thermal or regional metamorphism. The Hayachine ultramafic complex (2 × 4 km) is located in the Hayachine tectonic belt in the Tohoku district, northeastern Japan. It experienced thermal metamorphism through the intrusion of the Cretaceous Tono granite (Fujimaki and Yomogida 1986a, 1986b). The Tari-Misaka (6 × 10 km) and Takase (2 × 3 km) ultramafic complexes are located in the Sangun zone of the Chugoku district, southwestern Japan. They lie in Paleozoic rocks and experienced thermal metamorphism from the intrusion of Cretaceous or Paleogene granitic rocks (Arai 1975; Matsumoto et al. 1995).

The serpentinites recrystallized to assemblages that contain olivine, tremolite, talc, anthophyllite, and enstatite. The following description and interpretation of the metamorphism are based on the work of Arai (1975), Fujimaki and Yomogida (1986a, 1986b), and Matsumoto et al. (1995), who noted the similarity in zoning to that described by Evans and Trommsdorff (1970). These relations are summarized in Figure 2. The anthophyllite in each complex had previously been identified based on composition and optical properties. It was estimated that the association anthophyllite-olivine formed by reaction 1 (Arai 1975; Fujimaki and Yomogida 1986a, 1986b; Matsumoto et al. 1995). In the Hayachine ultramafic complex, anthophyllite also occurs with metamorphic enstatite and may have formed by the reverse of reaction 2 (Fujimaki and Yomogida 1986b).

We examined amphiboles reported as anthophyllite from each of the complexes. The samples were collected along the Komegamori stream at an elevation of 1230 m in the Hayachine ultramafic complex, along an unnamed stream between the Shirataki mountain and Takao at an elevation of 640 m in the Tari-Misaka ultramafic complex, and in a waste dump (drill-core samples) at the closed Takase chromite mine in the Takase ultramafic complex.

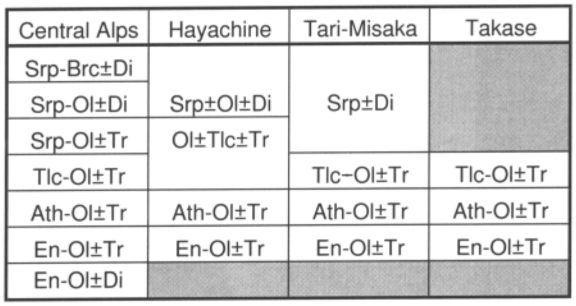

Central Alps	Hayachine	Tari-Misaka	Takase
Srp-Brc±Di	Srp±Ol±Di Ol±Tlc±Tr	Srp±Di	▨
Srp-Ol±Di			
Srp-Ol±Tr			
Tlc-Ol±Tr		Tlc–Ol±Tr	Tlc-Ol±Tr
Ath-Ol±Tr	Ath-Ol±Tr	Ath-Ol±Tr	Ath-Ol±Tr
En-Ol±Tr	En-Ol±Tr	En-Ol±Tr	En-Ol±Tr
En-Ol±Di	▨	▨	▨

FIGURE 2. Critical mineral assemblages of metamorphosed serpentinites, based on the descriptions of Evans and Trommsdorff (1970), Arai (1975), Fujimaki and Yomogida (1986a, 1986b), and Matsumoto et al. (1995). Temperature increases toward the bottom of the figure. Shadowed areas indicate missing assemblages. Diopside and tremolite occur in Ca-bearing serpentinites. Ath = anthophyllite, Brc = brucite, Di = diopside, En = enstatite, Ol = olivine, Srp = serpentine, Tlc = talc, and Tr = tremolite.

TABLE 1. Simulation conditions for protoanthophyllite (Path), anthophyllite (Ath), and cummingtonite (Cum)

	Microscope parameters			
Operating Voltage	400 kV	200 kV		
Cs	1.0 mm	2.0 mm		
robj	5 nm^{-1}	4 nm^{-1}		
Δ	7 nm	7.5 nm		
θ	0.4 mrad	0.5 mrad		
Scherzer focus	–40.5 nm	–70.8 nm		
		Structural Data		
		Path	Ath	Cum
Space group		*Pnmn*	*Pnma*	*C2/c*
Cell dimensions	*a (nm)*	0.9425	1.8524	0.951
	b (nm)	1.8303	1.7975	1.819
	c (nm)	0.5345	0.528	0.533
	β (°)			101.92
Composition		$\mathrm{Mg_7Si_8O_{22}(OH)_2}$		
	Slice Thickness			
[100]	**a**/2	**a**/4	–	
[301]	–	–	[301]/6	
[010]	**b**/4	**b**/4	**b**/4	
[001]	**c**	**c**	**c**	
[101]	–	[101]/4	–	
[201]	[201]/4	–	–	
[110]	[110]/5	[110]/5	[110]/5	

Notes: Cs = spherical aberration coefficient; robj = objective aperture radius; Δ = defocus spread; and θ = beam divergence.

EXPERIMENTAL METHODS

Specimens for HRTEM observation were prepared by crushing or ion milling. Selected crystals were crushed in an agate mortar under isopropyl alcohol and ultrasonicated for a few minutes. Others were immersed in isopropyl alcohol and crushed between two glass slides. A drop of the resulting suspension was placed onto lacey-carbon film supported by a standard Cu transmission electron microscope (TEM) grid and air-dried. Specimens for ion milling were prepared by cutting from petrographic thin sections, polishing until they were 20 μm thick, and mounting onto Mo TEM grids. We thinned the samples with a Gatan Inc. model 691 Precision Ion Polishing System ion mill. Initial thinning was at a voltage of 4.5 kV and an incident ion-beam angle of 6°, followed by more gentle milling at a voltage at 2 kV and an incident angle of 3°. The ion-milled specimens were lightly carbon coated.

Most HRTEM and SAED measurements were done with a JEOL 4000EX TEM operated at 400 kV (point-to-point resolution 0.17 nm and spherical aberration coefficient Cs = 1.0 mm). [011] HRTEM observations of the Takase samples and SAED measurements of the Tari-Misaka samples were done using a JEOL 2000FX TEM operated at 200 kV (point-to-point resolution 0.28 nm and Cs = 2.0 mm). HRTEM images were recorded near Scherzer defocus [$\Delta f = -(Cs\lambda)^{1/2}$], and the exact defocus values corresponding to the observed images were determined by comparing them to the simulated images. All images were digitized by using a film scanner at 3K dpi resolution. The images were Fourier-filtered using Digital Micrograph version 2.5 (Gatan Inc.).

We simulated HRTEM images of the *Pnmn*, *Pnma*, and *C*2/*m* polymorphs to explore the conditions for which interpretable micrographs of the stacking sequences might be obtained. We also simulated electron-diffraction patterns to differentiate the intensity distributions among the various polymorphs. The simulations were done using the multislice algorithm as implemented in the CERIUS program version 4.0 (Molecular Simulation Inc.) at the conditions summarized in Table 1. Atomic coordinates were from structure data sets of cummingtonite (Ghose 1961), anthophyllite (Finger 1970), and protomanganoferro-anthophyllite (Sueno et al. 1998). We used Mg in place of Fe and Mn in the published data, did not use thermal factors in the calculations, and ignored H. We generated models for protoanthophyllite with the following compositions: (1) Mg end-member, (2) 10% Fe in each octahedral site, and (3) 35% Fe in the M4 site. The intensity distributions of electron-diffraction patterns differ slightly among these models, but the simulated HRTEM images appear identical. In this paper, we compare simulated images and electron-diffraction patterns for Mg end-members. The simulations were done for integral numbers of unit cells. Thickness values given in the captions have been rounded. The thicknesses of the observed specimens were determined by comparing them to simulated images.

The compositions of individual crystals were determined using electron microprobe analysis (EMPA). These analyses were done with a JEOL JXA-8600SX instrument using wavelength-dispersive spectrometry at an accelerating voltage of 15 kV, a 10 nA beam current, and a ~1 μm beam diameter. Data reduction was done using standard ZAF matrix correction procedures. Element-distribution maps (500 × 500 pixels; 1 pixel = $0.25 \times 0.25\ \mu\mathrm{m}^2$) were generated using a JEOL JXA-8800M instrument at an accelerating voltage of 15 kV and a 65 nA beam current. Data were collected for 50 ms/pixel in the wavelength-dispersive mode.

Powder XRD patterns were obtained using a Rigaku/Max-IIB diffractometer and a diffracted-beam, curved-graphite monochromator. Each scan used a 0.02° step size and a counting time of 1 second per step, with samples placed onto a zero-background quartz plate. The powder XRD patterns of Mg end-members of protoanthophyllite and anthophyllite were calculated using CERIUS program version 4.0 and published structural data sets (Finger 1970; Sueno et al. 1998). Optical properties were measured using a universal stage (Nichika Co.) attached to a polarizing microscope.

OPTICAL MICROSCOPY, EMPA, AND XRD

The samples from all three localities were identified as protoanthophyllite using SAED and HRTEM measurements; however, their modes of occurrence and optical properties are similar to those of anthophyllite. Protoanthophyllite occurs as prismatic crystals with maximum lengths of 2 mm, 5 mm, and 1 cm along the **c** axis in samples from Hayachine, Takase, and Tari-Misaka, respectively. In some cases, protoanthophyllite crystals occur in radial aggregates. The protoanthophyllite and anthophyllite have the same optical orientations: $X = \mathbf{a}$, $Y = \mathbf{b}$, $Z = \mathbf{c}$. The optic axial angle of protoanthophyllite, $2V_x = 64 \pm 5°$, is within experimental error of the anthophyllite value reported by Evans et al. (2001). The protoanthophyllite is colorless in thin sections.

The protoanthophyllite from all three localities is associated with olivine, talc, serpentine minerals, chlorite, chromian spinels, magnetite, and calcite. The Hayachine protoanthophyllite is also associated with enstatite, tremolite, and pentlandite; and the Takase protoanthophyllite is associated with pentlandite. In some cases, protoanthophyllite crystals contain wide-chain (010) pyribole lamellae that range from one to several tens of micrometers in width, and anthophyllite lamellae parallel to (100) that range from one to several micrometers across. The enstatite associated with the Hayachine protoanthophyllite is free of exsolution lamellae on the scale of optical microscopy and is characterized by low Ca contents. These features indicate the enstatite is not a relic of primary peridotite or harzburgite, but a recrystallization product of serpentinite (Evans and Trommsdorff 1974; Springer 1974; Arai 1975). In the Hayachine samples, the protoanthophyllite crystals cut through large metamorphic enstatite grains (Figs. 3a, 3b, and 3c), suggesting that the protoanthophyllite formed after the enstatite. Calcite occurs as fine veins in all samples and in places cuts across anthophyllite.

The compositions of protoanthophyllite and anthophyllite are identical within experimental error; both polymorphs have a high Mg/(Mg + Fe) ratio (Table 2). However, they are distinguishable from one another in back-scattered electron images. Anthophyllite lamellae show slightly brighter contrast than

TABLE 2. Compositions of protoanthophyllite and anthophyllite (Ath)

Wt%	Hayachine	Tari-Misaka	Takase	Takase (Ath)
SiO_2	59.27	58.77	58.37	58.51
TiO_2	0.00	0.00	0.01	0.03
Al_2O_3	0.16	0.84	0.95	0.79
Cr_2O_3	0.04	0.01	0.03	0.00
FeO	6.19	5.17	5.40	5.69
MnO	0.15	0.15	0.11	0.10
NiO	0.07	0.18	0.11	0.07
MgO	31.10	32.24	31.43	31.06
CaO	0.15	0.01	0.00	0.02
Na_2O	0.07	0.12	0.29	0.17
K_2O	0.00	0.00	0.00	0.01
H_2O	2.23	2.24	2.22	2.22
Total	99.43	99.73	98.92	98.67
23 oxide anions				
Si	7.98	7.87	7.88	7.92
Ti	0.00	0.00	0.00	0.00
Al	0.03	0.13	0.15	0.13
Cr	0.00	0.00	0.00	0.00
Fe	0.70	0.58	0.61	0.64
Mn	0.02	0.02	0.01	0.01
Ni	0.01	0.02	0.01	0.01
Mg	6.24	6.43	6.33	6.27
Ca	0.02	0.00	0.00	0.00
Na	0.02	0.03	0.08	0.04
K	0.00	0.00	0.00	0.00
Total	15.02	15.08	15.07	15.02
Mg/(Mg+Fe)	0.90	0.92	0.91	0.91

Notes: H_2O percentages were calculated assuming the amphibole has an ideal composition. All Fe was calculated as Fe^{2+}.

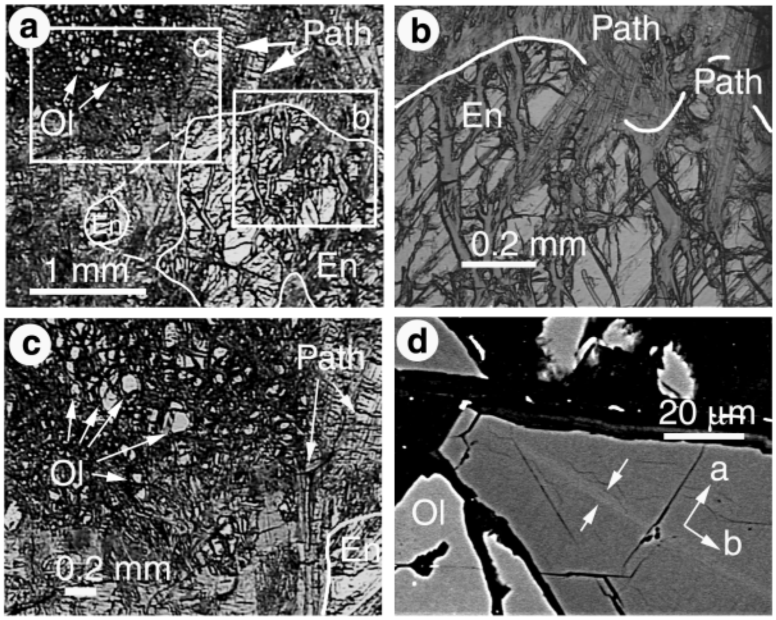

FIGURE 3. (**a**) Transmitted light photomicrograph of Hayachine protoanthophyllite (Path = acicular), enstatite (En = large light grain), and olivine (Ol = fine grained fragments). The solid and dashed white lines respectively indicate the observed and estimated enstatite grain boundaries. (**b, c**) Enlarged views of the boxed areas in **a**. (**d**) Back-scattered electron image of Takase protoanthophyllite. A 5 μm wide (100) anthophyllite lamella (between arrows) shows lighter contrast. Materials that have dark contrast around the olivine and protoanthophyllite are serpentine, talc, and chlorite.

those of protoanthophyllite (Fig. 3d). Although the evidence is not as strong as we would like, chemical mapping with an electron microprobe suggests that the anthophyllite may have a slightly higher Ca content.

The cell dimensions of anthophyllite and protoanthophyllite are almost identical, except that $\mathbf{a}_{\mathrm{ath}} = 2\mathbf{a}_{\mathrm{path}}$. A result is that the diffraction pattern of protoanthophyllite is almost identical to that of anthophyllite, although slight differences in peak intensities exist, and anthophyllite exhibits a few extra peaks. Because of these similarities it is difficult to distinguish between the two minerals with XRD measurements, especially if, as is typical of our samples, the protoanthophyllite is intergrown with anthophyllite and other minerals.

TEM RESULTS

Our samples, like those of *C*2/*m* cummingtonite, are characterized by $h + k = 2n + 1$ extinctions in [001] SAED patterns (Figs. 4a and 4d), but they exhibit minor differences from anthophyllite [001] patterns (Fig. 5). Differences among the various polymorphs are evident for reflections in the first-order Laue zone. Our samples are all characterized by a lack of systematic extinctions in the *hk*1 reflections, and their relative positions indicate $\beta = 90°$ (Figs. 4b and 4c). The patterns show they have a primitive orthorhombic unit cell with $a \approx 0.9$ and $b \approx 1.8$ nm, which is consistent with protoanthophyllite but not anthophyllite or cummingtonite (*C*2/*m* and $P2_1/m$).

The [100] SAED patterns of our samples are characterized by $k + l = 2n + 1$ extinctions with $b \approx 1.8$ and $c \approx 0.53$ nm (Fig. 6, top), and so are consistent with both protoanthophyllite and anthophyllite (Fig. 7, top). However, we can distinguish between them by measuring [201] SAED patterns of protoanthophyllite or [101] SAED patterns of anthophyllite. Anthophyllite has twice the *a* dimension of protoanthophyllite, resulting in unique $-1kl$ and $-3k3$ reflections that are absent in protoanthophyllite. Simulated electron-diffraction patterns for

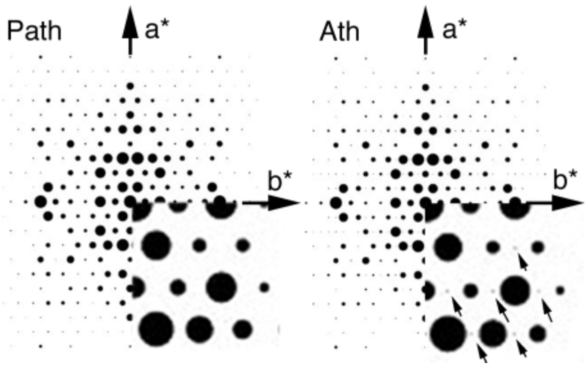

FIGURE 5. Simulated [001] electron-diffraction patterns of protoanthophyllite (Path) and anthophyllite (Ath). Simulation thicknesses are ~11 nm. Enlargements are inserted in the lower-right corners. Anthophyllite reflections with $h = 4n$, $k = 2n + 1$ and $h = 4n + 2$, $k = 2n$ (arrows in the insert) appear, but the intensities are weak. The corresponding reflections for protoanthophyllite are extinct.

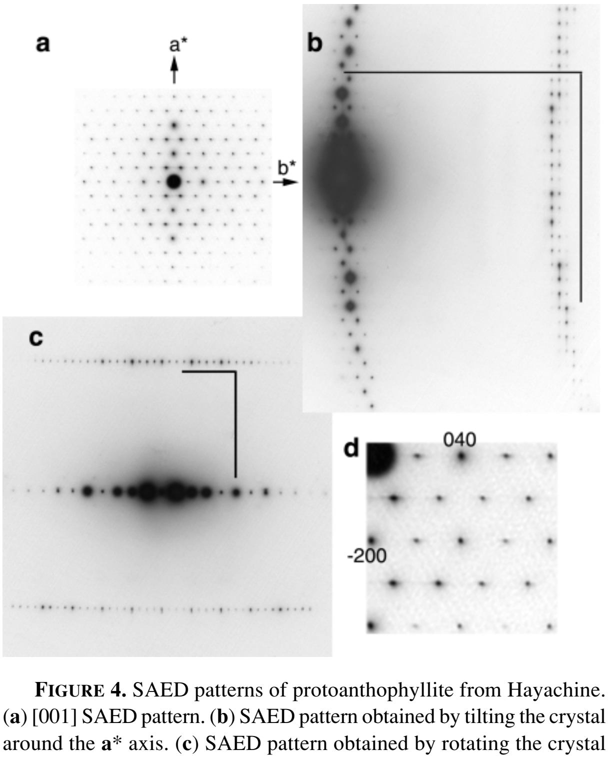

FIGURE 4. SAED patterns of protoanthophyllite from Hayachine. (**a**) [001] SAED pattern. (**b**) SAED pattern obtained by tilting the crystal around the **a*** axis. (**c**) SAED pattern obtained by rotating the crystal around the **b*** axis. (**d**) Enlargement of the SAED pattern in **a**. The inverted L symbols in **b** and **c** are given to indicate reference 90° angles.

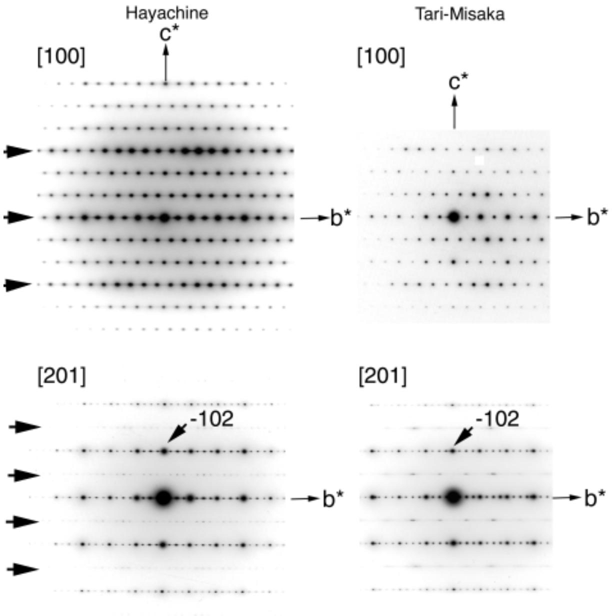

FIGURE 6. The [100] and [201] SAED patterns of protoanthophyllite from Hayachine (left column) and Tari-Misaka (right column). The [201] SAED patterns (bottom) are obtained by rotation of ~16° around the **a*** axis from the [100] orientation (top). 0*k*0 and 0*k*3 reflections (arrows in upper figure) are stronger than the reflections in the other rows. Weak diffuse streaks parallel to **b*** result from small amounts of chain-width disorder.

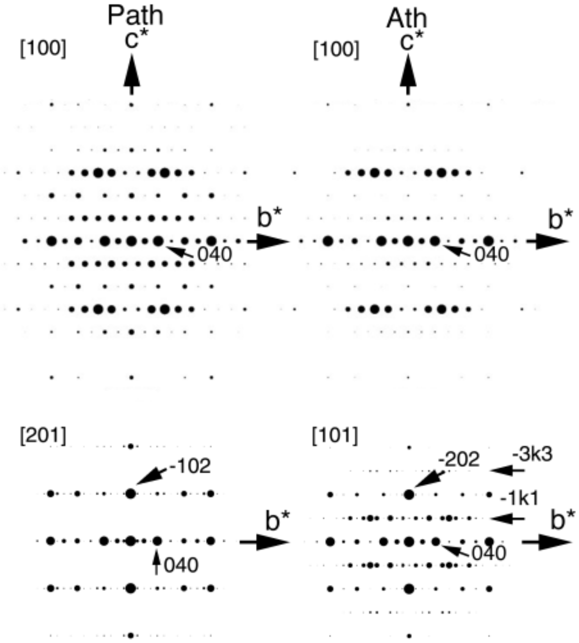

FIGURE 7. Simulated [100] and [201] electron-diffraction patterns of protoanthophyllite (Path) and [100] and [101] patterns of anthophyllite (Ath). Simulation thicknesses are ~11 nm for [100] projections and ~12 nm for Path [201] and Ath [101]. Path [201] is parallel to Ath [101]. The –1*k*1 Ath reflections (lower right) are stronger than the reflections in the other upper rows in the simulated Ath [101] pattern. The simulated Path [201] electron-diffraction pattern (lower left) does not have any reflections between the –1*k*2 and 0*k*0 reflections. Kinematically forbidden 0*k*0 reflections with $k = 2n + 1$ for the *Pnmn* space group occur in the calculated diffraction patterns (lower-left pattern).

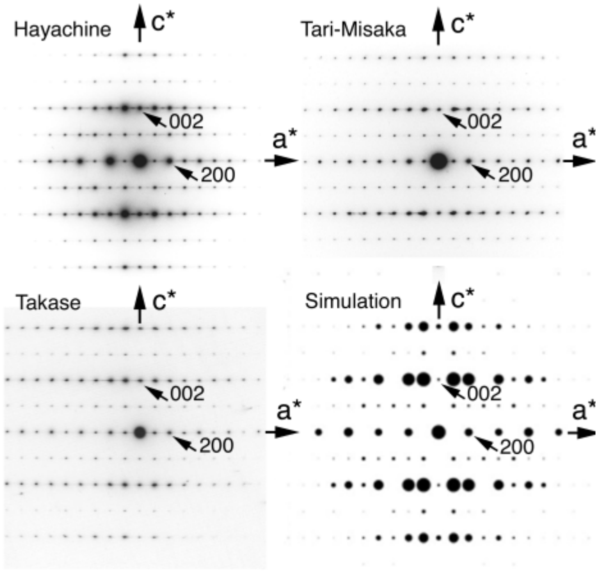

FIGURE 8. [010] SAED patterns of protoanthophyllite from Hayachine, Tari-Misaka, and Takase. A simulated [010] pattern of protoanthophyllite with an ~11 nm thickness is shown in the lower right. All patterns have 0.9^{-1}nm^{-1} a* spacings, indicating they are from protoanthophyllite. 00*l* reflections with $l = 2n + 1$ and *h*00 reflections with $h = 2n + 1$ occur, although they are kinematically forbidden for the *Pnmn* space group. These reflections do not appear in the simulated pattern with a perfect orientation (lower right), but they do appear if we impart a slight tilt to our simulations.

anthophyllite predict strong intensities for these reflections (Fig. 7, lower right). The observed reflections of our samples at the positions that correspond to the –1*k*1 and –3*k*3 anthophyllite reflections are absent or weak (arrows, Fig. 6, bottom), indicating that the principal phase has a 0.9 nm *a* dimension, which is consistent with that of protoanthophyllite.

[010] SAED patterns are characterized by rectangular net patterns with the 0.9^{-1}nm^{-1} **a*** spacings of proto-anthophyllite or the 1.8^{-1}nm^{-1} **a*** spacings of anthophyllite, or $\beta \approx 78°$ for monoclinic polymorphs and so are useful for distinguishing among them. The [010] SAED patterns of specimens from all three Japanese localities are characterized by rectangular net patterns with $\sim 0.9^{-1}\text{nm}^{-1}$ along **a*** (Fig. 8), indicating they are protoanthophyllite.

In [010] projections, each polymorph has a unique relative position of SiO_4 tetrahedra and (Mg, Fe)-centered octahedral sites, resulting in distinctive HRTEM images. In the calculated projected-potential images, Si and superimposed O positions of SiO_4 tetrahedra, and (Mg, Fe)-centered octahedral sites give strong intensities (Fig. 1, middle column), and the linkages of these positions produce wavy or linear dark contrast in the simulated HRTEM images (Fig. 1, right column). The protoanthophyllite HRTEM image has a sinusoidal variation with a wavelength of 0.9 nm along the **a** axis.

The observed [010] HRTEM images are characterized by sinusoidal contrast with wavelengths of 0.9 nm along **a**, similar to that in thin areas (less than ~20 nm) of images of protoanthophyllite simulated near Scherzer defocus (Figs. 1, 9, and 10). Many experimental [010] images show faint symmetry-forbidden fringes with 0.9 nm spacings. These fringes are artifacts of crystal or beam tilt, consistent with the results of Smith et al. (1983, 1985).

Each polymorph also has unique HRTEM images in [011] projection, as illustrated by Bozhilov and Evans (2001) for Fe-rich amphiboles. In such orientations, atoms in tetrahedral layers are localized so that regions with high and low charge density alternate parallel to tetrahedral layers. In simulated [011] images of Mg-rich amphiboles, regions with high charge density appear as dark dots at underfocus conditions (Fig. 11b). In such projections we can distinguish among the various amphibole polymorphs and thereby provide additional evidence that our samples are protoanthophyllite. (Fig. 11a).

The SAED patterns of our samples from Hayachine, Tari-Misaka, and Takase are characterized by the presence of all *hkl* and *h*0*l* reflections, *hk*0 reflections for only $h + k = 2n$, and 0*kl* reflections for $k + l = 2n$, requiring that the space group is *Pnmn* or *Pn*2*n*.

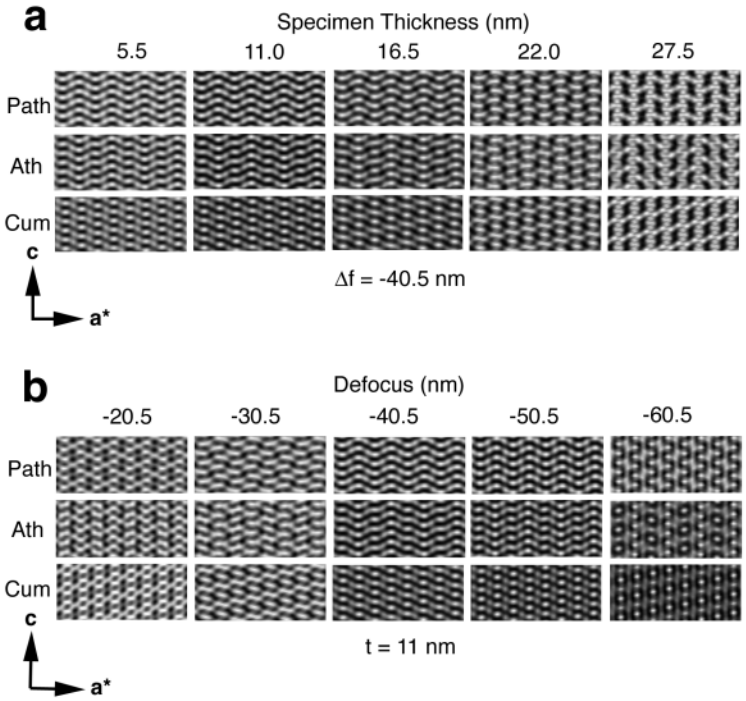

FIGURE 9. Simulated [010] HRTEM images with 0.2 nm resolution of protoanthophyllite (Path; $4a \times 3c$), anthophyllite (Ath; $2a \times 3c$), and $C2/m$ cummingtonite (Cum; $4a \times 3c$) as functions of specimen thickness and defocus. (**a**) Thickness dependence of [010] HRTEM images of amphiboles. A defocus value of –40.5 nm is used. If the thickness is greater than ~20 nm, the HRTEM images are too complicated to recognize the stacking sequences of the tetrahedral layers. (**b**) Defocus dependence of [010] HRTEM images of amphiboles. A thickness (t) of ~11 nm is assumed. The [010] HRTEM image of protoanthophyllite is characterized by sinusoidal contrast with a wavelength of 0.9 nm along the **a** axis near Scherzer defocus (–40.5 nm), whereas [010] HRTEM images of the other polymorphs do not show such contrast. Also, see the right column of Figure 1.

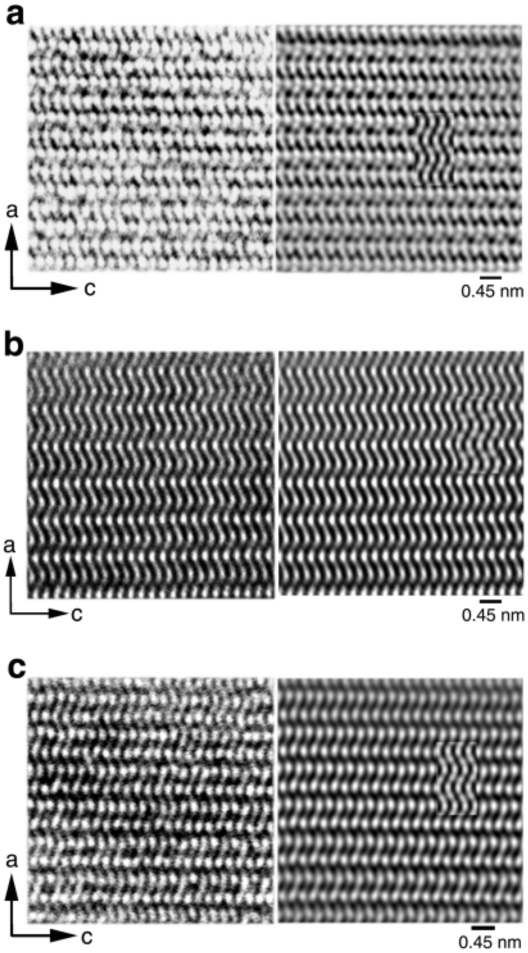

◀ **FIGURE 10.** [010] unfiltered (left) and Fourier-filtered (right) HRTEM images of protoanthophyllite from (**a**) Hayachine, (**b**) Tari-Misaka, and (**c**) Takase. The inserts on the right are of simulated images ($2a \times 2c$) with a specimen thickness of ~11 nm and a defocus value of –40.5 nm.

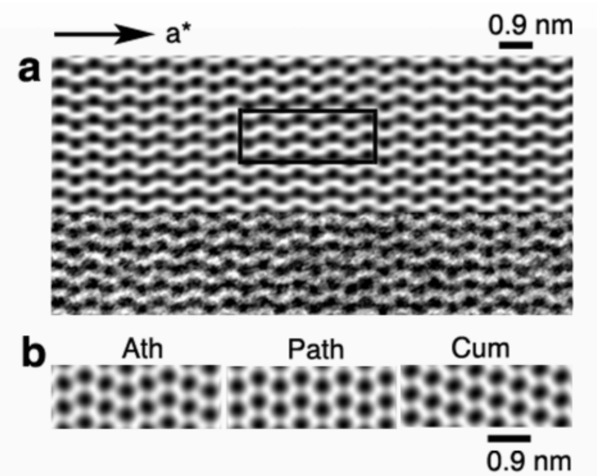

FIGURE 11. (**a**) [011] Fourier-filtered (top) and unfiltered (bottom) HRTEM images of protoanthophyllite from the Takase serpentinite and (**b**) simulated HRTEM images of anthophyllite (Ath), protoanthophyllite (Path), and cummingtonite (Cum). The simulation thickness is ~19 nm and a defocus value of –70.8 nm was used. The simulated images have the same size as the boxed area in **a**.

DISCUSSION

In the types of intergrowths in which most of our protoanthophyllite samples occur the recognition of protoanthophyllite requires either single-crystal XRD, SAED, or HRTEM measurements. However, the identification of anthophyllite in published studies of both natural and synthetic samples is based on none of these methods. A result is that some of the identifications in the literature could be incorrect. By analogy with anthophyllite, the recognition of gedrite may also be in question. It remains to be determined whether such misidentifications occur and, if they do, whether they make a difference in interpreting *P-T* conditions. If, like anthophyllite and cummingtonite, protoanthophyllite and anthophyllite only differ by roughly 2 or 3 kJ/mol in free energy, they will only impact dehydration reactions by ~10 or 20 °C (Evans, personal communication, 2001).

It is not known whether protoanthophyllite has a true stability field, although Bozhilov and Evans (2001) discussed the possibility that protoferro-anthophyllite is a stable phase. An answer may lie in the modes of occurrence of protoanthophyllite. Judging from the mineral assemblages of the samples and metamorphic zonation described by previous workers (Arai 1975; Fujimaki and Yomogida 1986a, 1986b; Matsumoto et al. 1995), protoanthophyllite from Hayachine, Tari-Misaka, and Takase may have formed by the reaction:

$$4 \text{ olivine} + 9 \text{ talc} = 5 \text{ protoanthophyllite} + 4 \text{ H}_2\text{O} \qquad (3)$$

or inversion of anthophyllite that was produced by reaction 1. The Hayachine sample reached temperatures above ~650 °C based on the *P-T* diagram of Spear (1993), and metamorphic enstatite possibly formed by reaction 2 or 4:

$$\text{protoanthophyllite} + \text{olivine} = 9 \text{ enstatite} + \text{H}_2\text{O}. \qquad (4)$$

Some protoanthophyllite crystals from Hayachine formed after metamorphic enstatite so that some or all proto-anthophyllite crystals may have formed by the reverse of reaction 4 or inversion of anthophyllite produced by reaction 2. If the protoanthophyllite is not an inversion product of anthophyllite, protoanthophyllite instead of anthophyllite may have formed around 600–700 °C. The fact that proto-anthophyllite occurs in three different metamorphosed serpentinites and may have formed by prograde and retrograde reactions raises the possibility that protoanthophyllite has a true stability field.

ACKNOWLEDGMENTS

We thank Bernard Evans for initial review of this manuscript and Alain Baronnet and an anonymous reviewer for formal reviews. We also thank Satoshi Nakano for element mapping of our samples and Hirokazu Fujimaki and Kunihiko Yomogida for providing a copy of an unpublished geological map of the Hayachine ultramafic complex. Electron microscopy was done at the Center for High Resolution Electron Microscopy at Arizona State University. Funding was provided by NSF grant EAR-0003533.

REFERENCES CITED

Arai, S. (1975) Contact metamorphosed dunite-harzburgite complex in the Chugoku District, western Japan. Contributions to Mineralogy and Petrology, 52, 1–16.

Bozhilov, K.N. and Evans, B.W. (2001) Ferroanthophyllite in Rockport grunerite: A transmission electron microscopy study. American Mineralogist, 86, 1252–1260.

Deer, W.A., Howie, R.A., and Zussman, J. (1997) Rock Forming Minerals, Volume 2B, Double-Chain Silicates, 764 p. The Geological Society, London.

Evans, B.W. and Trommsdorff, V. (1970) Regional metamorphism of ultramafic rocks in the Central Alps: Parageneses in the system CaO-MgO-SiO_2-H_2O. Schweizerische Mineralogische und Petrographische Mitteilungen, 50, 481–492.

Evans, B.W. and Trommsdorff, V. (1974) Stability of enstatite + talc, and CO_2 -metasomatism of metaperidotite, Val d'Efra, Lepontine Alps. American Journal of Science, 274, 274–296.

Evans, B.W., Ghiorso, M.S., Yang, H., and Medenbach, O. (2001) Thermodynamics of the amphiboles: Anthophyllite-ferroanthophyllite and the ortho-clino phase loop. American Mineralogist, 86, 640–651.

Finger, L.W. (1970) Refinement of the crystal structure of an anthophyllite. Year Book Carnegie Institution of Washington, 283–288.

Fujimaki, H. and Yomogida, K. (1986a) Petrology of Hayachine ultramafic complex in contact aureole, NE Japan. (I) Primary and metamorphic minerals. Journal of the Japanese Association of Mineralogists, Petrologists and Economic Geologists, 81, 1–11.

———(1986b) Petrology of Hayachine ultramafic complex in contact aureole, NE Japan. (II) Metamorphism and origin of the complex. Journal of the Japanese Association of Mineralogists, Petrologists and Economic Geologists, 81, 59–66.

Ghose, S. (1961) The crystal structure of a cummingtonite. Acta Crystallographica, 14, 622–627.

Gibbs, G.V. (1969) Crystal structure of protoamphibole. Pyroxenes and amphiboles—Crystal chemistry and phase petrology. Mineralogical Society of America special paper 2, 101–109.

Gibbs, G.V., Bloss, F.D., and Shell, H.R. (1960) Proto-amphibole, a new polytype. American Mineralogist, 45, 974–989.

Hawthorne, F.C. (1981) Crystal chemistry of the amphiboles. In D.R. Veblen, Ed. Amphiboles and Other Hydrous Pyriboles: Mineralogy, 9a, p. 1–102. Reviews in Mineralogy, Mineralogical Society of America, Washington, D.C.

Leake, B.E., Woolley, A.R., Arps, C.E.S., Birch, W.D., Gilbert, M.C., Grice, J.D., Hawthorne, F.C., Kato, A., Kisch, H.J., Krivovichev, V.G., Linthout, K., Laird, J., Mandarino, J.A., Maresch, W.V., Nickel, E.H., Rock, N.M.S., Schumacher, J.C., Smith, D.C., Stephenson, N.C.N., Ungaretti, L., Whittaker, E.J.W., and Youzhi, G. (1997) Nomenclature of amphiboles: Report of the Subcommittee on Amphiboles of the International Mineralogical Association, Commission on New Minerals and Mineral Names. American Mineralogist, 82, 1019–1037.

Liu, J. and Liou, J.G. (1995) Kyanite-anthophyllite schist and southwest extension of the Dabie Mountains ultrahigh- to high-pressure belt. The Island Arc, 4, 334–346.

Matsumoto, I., Arai, S., Muraoka, H., and Yamauchi, H. (1995) Petrological characteristics of the dunite-harzburgite-chromite complexes of Sangun zone, Sowthwest Japan (in Japanese). Journal of the Japanese Association of Mineralogists, Petrologists and Economic Geologists, 90, 13–26.

Papike, J.J. and Ross, M. (1970) Gedrites: Crystal structures and intracrystalline cation distributions. American Mineralogist, 55, 304–305.

Robinson, P., Spear, F.S., Schumacher, J.C., Laird, J., Klein, C., Evans, B.W., and Doolan, B.L. (1982) Phase relations of metamorphic amphiboles: Natural occurrence and theory. In D.R. Veblen, and P.H. Ribbe, Eds., Amphiboles: Petrology and Experimental Phase Relations, 9B, p. 1–227. Reviews in Mineralogy, Mineralogical Society of America, Washington, D.C.

Smith, D.J., Saxton, W.O., O'Keefe, M.A., Wood, G.J., and Stobbs, W.M. (1983) The importance of beam alignment and crystal tilt in high resolution electron microscopy. Ultramicroscopy, 11, 263–282.

Smith, D.J., Bursill, L.A., and Wood, G.J. (1985) Non-anomalous high-resolution imaging of crystalline materials. Ultramicroscopy, 16, 19–31.

Spear, F.S. (1993) Metamorphic Phase Equilibria and Pressure-Temperature-Time Paths. 799 p. Mineralogical Society of America, Washington, D.C.

Springer, R.K. (1974) Contact metamorphosed ultramafic rocks in the western Sierra Nevada foothills, California. Journal of Petrology, 15, 160–192.

Sueno, S., Matsuura, S., Gibbs, G.V., and Boisen, M.B., Jr. (1998) A crystal chemical study of protoanthophyllite: orthoamphiboles with the protoamphibole structure. Physics and Chemistry of Minerals, 25, 366–377.

Thompson, J.B., Jr. (1970) Geometrical possibilities for amphibole structures: model biopyriboles. American Mineralogist, 55, 292–293.

Tracy, R.J. and Frost, B.R. (1991) Phase equilibria and thermobarometry of calcareous, ultramafic and mafic rocks, and iron formations. In D.M. Kerrick, Ed., Contact Metamorphism, 26, p. 207–289. Reviews in Mineralogy, Mineralogical Society of America, Washington, D.C.

Trommsdorff, V. and Evans, B.W. (1972) Progressive metamorphism of antigorite schist in the Bergell tonalite aureole (Italy). American Journal of Science, 272, 423–437.

MANUSCRIPT RECEIVED AUGUST 27, 2001
MANUSCRIPT ACCEPTED APRIL 20, 2002
MANUSCRIPT HANDLED BY ADRIAN J. BREARLEY